Volume 27
Number 34
14 September 2025
Pages 10037-10276

Green Chemistry

Cutting-edge research for a greener sustainable future

rsc.li/greenchem

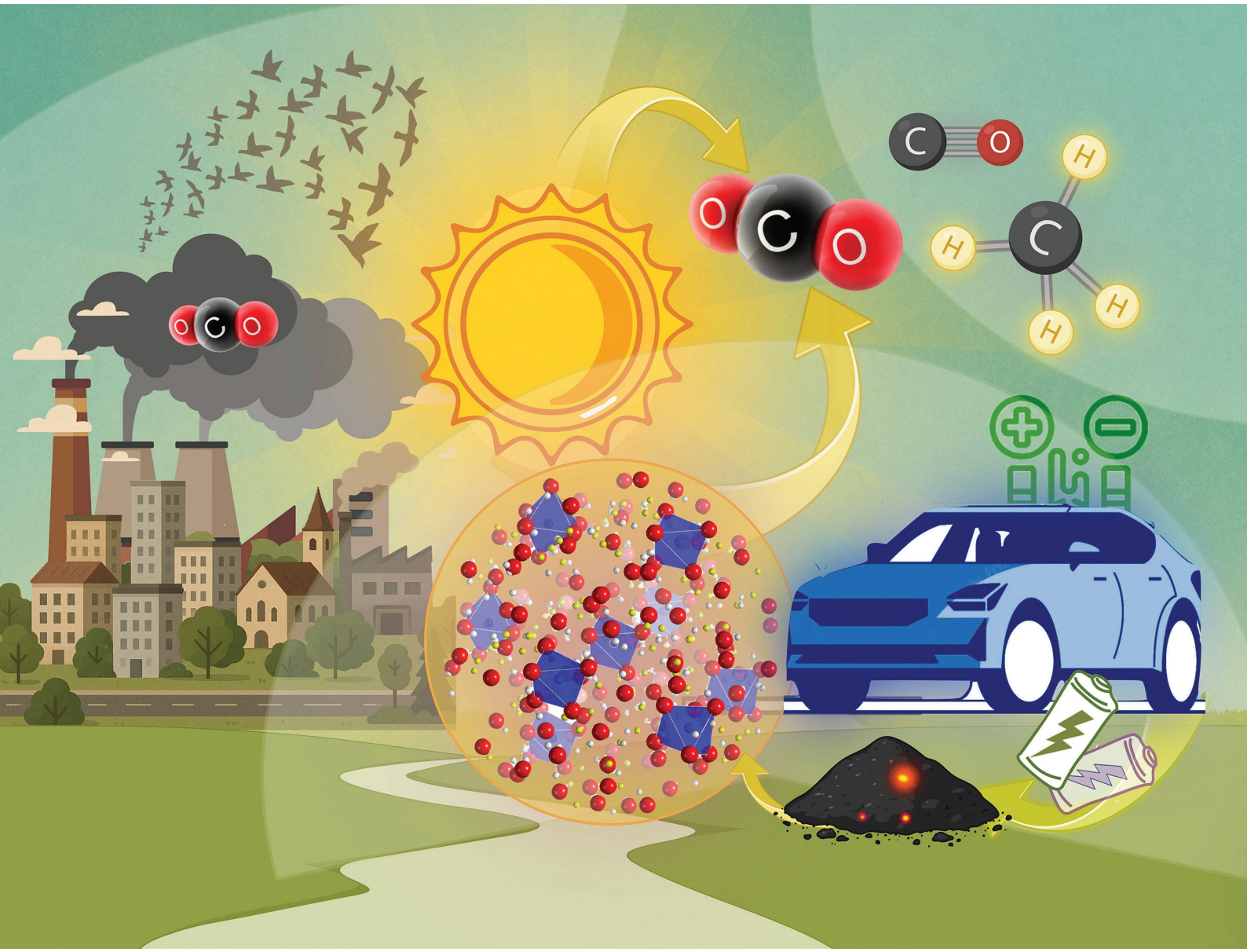

ISSN 1463-9262

ROYAL SOCIETY OF CHEMISTRY

PAPER

Roberto Fiorenza, Elza Bontempi *et al.*
Performance and structural evolution of a new critical raw material-free catalyst, synthesized from spent lithium-ion batteries, for solar-driven CO_2 conversion

25 YEARS ANNIVERSARY

Green Chemistry

PAPER

View Article Online
View Journal | View Issue

Cite this: *Green Chem.*, 2025, **27**, 10132

Performance and structural evolution of a new critical raw material-free catalyst, synthesized from spent lithium-ion batteries, for solar-driven CO_2 conversion

Antonella Cornelio,[a] Alessandra Zanoletti,[a] Giusy Dativo,[b] Roberto Fiorenza,*[b] Annalisa Zacco,[a] Mohsin Muhyuddin,[c] Carlo Santoro,[c] Laura E. Depero [a] and Elza Bontempi *[a]

Received 23rd May 2025,
Accepted 21st July 2025

DOI: 10.1039/d5gc02583d

rsc.li/greenchem

The development of next-generation catalysts is crucial for advancing sustainable CO_2 conversion technologies and addressing pressing environmental challenges. This work integrates green chemistry principles by combining CO_2 valorization, waste recovery, and renewable energy use, demonstrating a sustainable and circular approach for catalyst discovery and application. This study investigates the functional and structural properties of a novel malate-based catalyst synthesized starting from spent lithium-ion battery waste, developed after lithium recovery. Under solar photothermo-catalytic conditions, the catalyst showed excellent CO_2-to-solar fuel conversion (CO and CH_4) at low temperature, with a higher CH_4 selectivity (>80%) compared to classical catalysts based on critical raw materials. X-ray pair distribution function analysis was used for the first time to reveal a significant structural transformation: the catalyst undergoes a transition from a crystalline resting state to an amorphous, catalytically active shell during the reaction, significantly enhancing the material efficiency. A preliminary sustainability analysis shows that the embodied energy and carbon footprint values associated with the synthesis of the new malate are comparable with those of the classical catalysts used for this application, based on ceria, titania, and bismuth.

Green foundation

1. This study presents a new alternative to critical raw material-based catalysts that are able to decompose CO_2.
2. The recovery and reuse of waste materials from spent batteries support greenhouse gas reduction and the circular economy with a new sustainable technology.
3. The use of solar irradiation to drive CO_2 conversion at low temperatures points toward a cost-effective and carbon-neutral process for producing valuable fuels and chemicals.

1. Introduction

The increasing concentration of atmospheric CO_2, which has recently exceeded 400 ppm,[1] due to anthropogenic activities has led to global climate concerns, necessitating the development of renewable alternative energy sources and more effective CO_2 conversion technologies.

The development of efficient, cost-effective, and environmentally sustainable energy storage systems—particularly lithium-ion batteries—has become increasingly critical to advancing the transition toward a low-carbon energy future. While lithium-ion batteries play a key role in enabling renewable energy integration and electric mobility, their long-term sustainability is limited by the low efficiency and scalability of current recycling technologies. Recovery rates for critical raw materials (CRMs) such as lithium remain relatively modest, and existing recycling processes are often energy-intensive and environmentally taxing. In addition, the growing demand for raw materials to meet battery production needs raises concerns over resource depletion and potential geopolitical tensions.[2] Strengthening the recyclability of lithium-ion batteries and developing closed-loop supply chains are therefore essen-

[a]*INSTM and Chemistry for Technologies Laboratory, Department of Mechanical and Industrial Engineering, University of Brescia, via Branze 38, 25123 Brescia, Italy. E-mail: elza.bontempi@unibs.it*
[b]*Department of Chemical Sciences, University of Catania, V.le A. Doria 6, Catania 95125, Italy. E-mail: roberto.fiorenza@unict.it*
[c]*Electrocatalysis and Bioelectrocatalysis Laboratory, Department of Materials Science, University of Milano-Bicocca, Via Cozzi 55, 20155 Milan, Italy*

tial steps to improve their overall environmental performance and secure the sustainability of the energy transition.

On the other hand, effective, sustainable, and efficient CO_2 conversion technologies, aiming to transform carbon dioxide into valuable products like fuels, chemicals, and building materials, face the challenge of developing economically viable solutions.[3]

Among various approaches, catalysis and photocatalysis have emerged as viable methods for CO_2 reduction with the possibility of its conversion into value-added products,[4–9] contributing to carbon neutrality and the circular economy.

The effectiveness of a catalyst depends on its composition, stability, and activity under reaction conditions. Moreover, in the last few years, the design of sustainable catalysts has gained considerable attention.[10,11] Photothermo-catalysis, which integrates photochemical and thermochemical processes, has recently shown to be a highly promising strategy for CO_2 conversion.[12] This approach efficiently harnesses solar energy while operating at lower temperatures compared to conventional thermocatalysis. At the same time, it achieves superior performance over both solar photocatalysis and thermocatalysis, making it a compelling solution for sustainable CO_2 transformation.[12] Several catalysts have been explored for this aim, each with its own set of advantages and limitations.[13] Titanium dioxide (TiO_2) is a widely used photocatalyst due to its strong oxidation ability, chemical stability, and low cost. It efficiently absorbs ultraviolet (UV) light, promoting photoreactions.[14] However, its wide band gap (~3.2 eV) limits its efficiency under visible light, requiring modifications or co-catalysts for enhanced performance.[15] Nickel-based catalysts (Ni) are cost-effective and highly active in thermocatalytic CO_2 conversion, particularly for the methanation reaction. However, these materials are prone to coking and deactivation over time, requiring additional support or promoters for long-term stability.[16] Copper-based catalysts (Cu) show good selectivity for CO production in CO_2 hydrogenation reactions and are relatively inexpensive, yet they suffer from low thermal stability and susceptibility to sintering at high temperatures. Ceria (CeO_2)-supported catalysts have excellent oxygen storage capacity, enhancing redox reactions and improving catalyst durability, but they come with high synthesis costs and potential sintering under extreme conditions. Perovskite oxides (*e.g.*, $LaFeO_3$ and $SrTiO_3$) exhibit tunable electronic structures, excellent stability, and strong catalytic activity under visible light, although they involve complex synthesis methods and relatively high production costs.[14]

Moreover, almost all these materials contain CRMs. The European Commission is actively promoting the substitution of certain CRMs as part of its broader strategy to reduce external dependencies and strengthen the EU's industrial resilience. Within the framework of the Critical Raw Materials Act, adopted in 2024, and considering geopolitical conditions,[2] substitution is identified as a key action to secure a sustainable and reliable supply of materials essential for the green and digital transitions. However, the substitution of CRMs remains a significant challenge, and to date, only a limited number of alternative materials have demonstrated real effectiveness.

The main aim of this work is to propose, for the first time, the use of spent LIBs to produce a new sustainable catalyst for CO_2 reduction, using solar photothermocatalytic conversion. In particular, the new material has been synthesized through a recently proposed carbothermic approach,[17,18] allowing us to obtain a new malate phase that was identified with the support of artificial intelligence (AI). AI also suggested the use of this new malate phase as a catalyst for CO_2 conversion.[17,19] The new catalyst presents a major advantage as it originates from waste, promoting a sustainable and circular economy. Another key advantage is that the material is derived from residuals remaining after lithium recovery, allowing the valorization of residual metals[18] other than lithium, a CRM, which is recovered in a preliminary recycling step. Finally, it is important to highlight that this material is essentially based on a nickel malate phase and does not incorporate CRMs. In particular, the EU strategic metals list includes nickel, but only battery-grade nickel, which refers to nickel of a purity suitable for battery production.[20]

This work combines several important innovations—not only through the development of a new material but also by presenting, for the first time, the integration of four key strategies aligned with green chemistry principles to promote sustainability in CO_2 reduction. First, it enables the transformation of CO_2 into renewable raw materials, advancing circular economy objectives. Second, it recovers waste from spent lithium-ion batteries to produce a novel catalyst, effectively turning waste into value. Third, the new catalyst is not based on CRMs, like titania or ceria. Finally, it leverages solar irradiation to drive low-temperature CO_2 conversion, offering a promising, low-cost, and carbon-neutral pathway for generating valuable fuels and industrial chemicals.

2. Experimental

2.1 Sample preparation

The malate was synthesized as recently reported,[21] by treating black mass originating from a spent NCM battery (with the general formula $LiNi_{1-x-y}Mn_xCo_yO_2$) following a new recycling technology that is able to separate and recover lithium in the first steps. The NCM sample was obtained from an industrial facility specialized in processing waste batteries from electric vehicles. Before its application, the material was mechanically pre-processed to eliminate plastic components and metal housings, followed by grinding the black mass into a fine powder and separating the fraction enriched in anodic and cathodic materials. The resulting powder was then sieved through a 300 μm mesh. The technology applied in this study is protected by patent PCT/IB2023/051034.

2.2 Materials and methods

The NCM sample, provided by Eneris Group from the industrial scale recycling plant in Zarki, Poland, was processed

using a PYRO Advanced Microwave Muffle Furnace (Milestone s.r.l., Bergamo, Italy) operating at 2.4 GHz and 1000 W for 10 minutes.[17] Following microwave treatment, the samples underwent water leaching to recover lithium. The remaining solid was then subjected to leaching with L-malic acid. After this step, the resulting solutions were stored in a refrigerator at 4 °C for approximately three weeks, allowing the precipitate to form. It resulted in a new malate phase.[21]

The new phase was digested to perform chemical analysis with the procedure reported in ref. 22.

Chemical analysis of the digested compound was performed by total X-ray fluorescence (TXRF) (instrument Horizon, by GNR, Italy) with a Mo anode and XRD patterns were collected using a PANalytical X'Pert Pro XRD (Malvern Panalytical, Almelo, Netherlands) at 40 mA and 45 kV, with Cu Kα1 radiation (λ = 1.54060 Å). SEM and EDS analyses were performed by optical microscopy (MZ16-A and MC190 HD, Leica microsystems).

The thermal profile of the sample from 25 °C to 1000 °C was observed through thermogravimetric analysis (TGA) combined with differential scanning calorimetry (DSC) using a STAR system (Mettler Toledo) in air with a heating rate of 10 °C min^{-1}.

High-resolution synchrotron X-ray diffraction and total scattering experiments were carried out at the ID31 beamline of the European Synchrotron Radiation Facility (ESRF). Powder samples were placed into cylindrical compartments (about 1 mm thick) secured between Kapton films within a high-throughput holder. Data acquisition was performed in transmission mode using an incident X-ray beam of 75.051 keV (λ = 0.16520 Å). The diffraction signals were captured using a Pilatus CdTe 2M detector (1679 × 1475 pixels, 172 × 172 μm^2 per pixel), positioned such that the beam hit the detector corner. The distance between the sample and detector was approximately 1.5 m for high-resolution scans and 0.3 m for total scattering measurements. Multiple measurements of the empty well with polyimide windows were measured and summed together for improved statistics for the background subtraction. The PDF plots were generated from the high-energy total-scattering diffraction data by using PDFgetX3.[23]

The textural properties of the sample were evaluated from N_2 adsorption–desorption measurements at −196 °C using a Micromeritics ASAP 2020 instrument. The Brunauer–Emmett–Teller (BET) method in the standard pressure range 0.05–0.3 p/p_0 was used to determine the BET surface area. The pore size distribution was evaluated with the Barrett–Joyner–Halenda (BJH) calculation method by analysis of the desorption curves. Before the measurements, the sample was degassed at 120 °C overnight.

The solar photothermocatalytic CO_2 conversion experiments were conducted in a cylindrical Pyrex batch reactor loaded with 0.2 g of catalyst material. The sample was pretreated overnight at 120 °C (the same temperature as the catalytic tests) to eliminate eventual impurities and the crystallization water. The system was illuminated for 5 hours using an Osram Ultra Vitalux 300 W solar lamp, providing an irradiance of 10.7 mW cm^{-2}. The setup was housed inside an insulated solar chamber, where the internal temperature stabilized at 120 °C, as continuously monitored and regulated using an IR camera. Prior to initiating the batch photothermocatalytic tests, the catalyst surface underwent a pre-cleaning process to remove potential carbon-based contaminants, following a previously established protocol.[24] In particular, the sample was left overnight under a He flow (30 cc min^{-1}) and UV irradiation (using a 100 W mercury lamp, Black-Ray B-100A, 365 nm) in order to desorb the possible contaminants and the carbonaceous species arising from the sample surface. Afterward, water vapour was introduced together with the He stream under irradiation and various portions of the gas leaving the reactor were analysed by gas chromatography (GC-TCD-FID) to monitor the effectiveness of the cleaning process and the possible presence of residual carbonaceous contamination. To ensure that the CO_2 converted during the catalytic tests and the evolved CO/CH_4 did not come from the examined sample, at the end of each photothermo-catalytic run, the batch reactor was opened, the sample was weighed to monitor any weight loss, and it was reused. The control measurement was repeated with water vapor and a He stream to verify whether the possible presence of CO/CH_4 or CO_2 evolved from the sample. Finally, several tests were performed, using both fresh and used samples, under the same experimental conditions of the CO_2 photothermo-catalytic measurements but without flowing CO_2. During all these control experiments, no other carbon sources, neither CO/CH_4 or CO_2, were detected.

For the CO_2 photothermo-catalytic tests, a CO_2 and H_2O vapor mixture was introduced into the photoreactor to ensure that the catalyst surface was fully saturated with reactant molecules. Water vapor was generated using a bubbler maintained at 80 °C. The CO_2/H_2O gas mixture was regulated through mass flow controllers to maintain a molar ratio of 15, promoting the CO_2 reduction pathway over the competing water splitting reaction.[25] The reaction products were analyzed using an Agilent 6890 N gas chromatograph equipped with an HP-PLOT Q column and a thermal conductivity detector (TCD). The formation of possible organic compounds (other than CO and CH_4) was realized by using a Trace GC instrument (Porapak Q column, FID detector).

After appropriate calibration with CO_2 standards, the values of CO_2 conversion were evaluated using eqn (1):

$$CO_2\ \text{conversion} = \left(\frac{(\text{area peak}\ CO_{2\,\text{in}} - \text{area peak}\ CO_{2\,\text{out}})}{\text{area peak}\ CO_{2\,\text{in}}}\right) \times 100 \quad (1)$$

The method of mass balance was also used to quantify the reaction outcomes using eqn (2):

$$CO_2\ \text{conversion} = \left(\frac{\text{area peak}\ CO_{2\,\text{out}}}{(\text{area peak products out} - \text{area peak}\ CO_{2\,\text{out}})}\right) \times 100 \quad (2)$$

The two reported methods resulted in a very good accordance with each other (±5%, reproducibility 95%).

The CO and CH_4 product selectivity with an electron basis was investigated by using the following formulae, eqn (3) and (4):

$$CH_4\ \text{selectivity}\,\% = \left(\frac{8N_{CH_4}}{(8N_{CH_4} + 2N_{CO})}\right) \times 100 \quad (3)$$

$$CO\ \text{selectivity}\,\% = \left(\frac{2N_{CO}}{(8N_{CH_4} + 2N_{CO})}\right) \times 100 \quad (4)$$

where N_{CH_4} and N_{CO} are the rates of the production of CH_4 and CO expressed in μmol $g_{catalyst}^{-1}$ $h_{irradiation}^{-1}$ and 2 and 8 are the coefficients representing the electrons involved in the photothermo-catalytic CO_2 conversion into CH_4 and CO, considering that the reductive agent is water (in accordance with the reactions (a) and (b)):

$$CO_2 + 2H^+ + 2e^- \rightarrow CO + H_2O, \quad (a)$$

$$CO_2 + 8H^+ + 8e^- \rightarrow CH_4 + 2H_2O. \quad (b)$$

All the values reported and the CO and CH_4 rates of formation have an experimental error of 3%.

Table 1 Metal composition in the malate material, identified by TXRF analysis, expressed as % [21]

Metal	%
Mn	1.16 ± 0.01
Co	3.21 ± 0.05
Ni	9.4 ± 0.1
Cu	0.96 ± 0.02

3. Results and discussion

The newly detected phase was used for photothermo-catalytic tests. The compound, with the formula $MH_2(C_4H_4O_5)_2{\cdot}4H_2O$, features a metal site (M) in an octahedral coordination environment. Structural analysis confirmed that the ligands consist of malate groups, which coordinate in a bidentate fashion, along with coordinated water molecules.[21] This configuration plays a fundamental role in the stability and catalytic activity of the material.

In Table 1, the metals (M) in the new malate were identified through TXRF. This analysis revealed that the material contains various metals, with nickel as the most abundant, along with cobalt, manganese, and copper, accounting for a total metal content of approximately 14.7%.

Fig. 1 shows the results of the thermal analysis of the sample pursued through TGA. The decomposition starts with two decomposition steps (85–230 °C) related to water evolution, corresponding to the release of the water molecules,[26] in accordance with the literature reporting that for manganese malate this occurs in the temperature range of 70–298 °C.[27] The first decomposition range (85–120 °C) can be attributed to the liberation of the crystallization water molecules. The second decomposition stage (190–230 °C) seems to correspond to the liberation of water molecules coordinated to the metallic ions.[26]

Fig. 2 illustrates the solar photothermo-catalytic activity of the examined sample for 5 runs (each run of 5 h of simulated solar irradiation at 120 °C).

In the reported experiments, only CO and CH_4 were detected as products of the solar photothermo-catalytic CO_2 reduction reaction. Interestingly, after the first run, the catalyst showed a good CO_2 conversion quantified at 64%. After 15 h of simulated solar irradiation at 120 °C (third run), the photo-

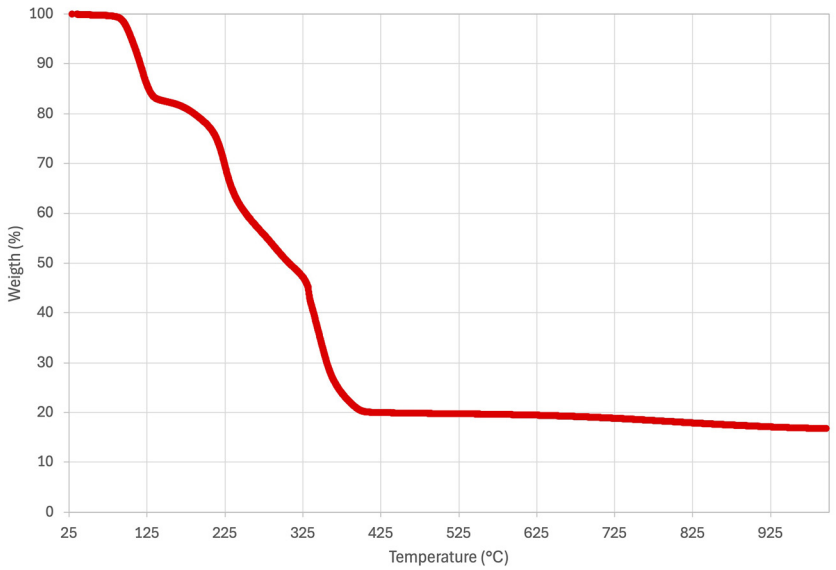

Fig. 1 The thermal profile of the malate sample obtained in air.

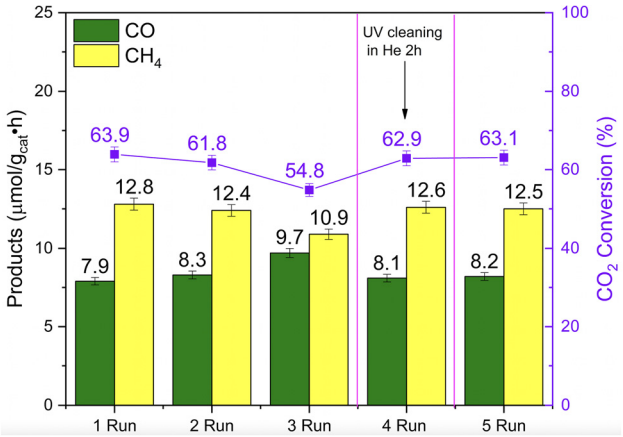

Fig. 2 Solar photothermo-catalytic tests for 5 runs (each run = 5 h of simulated solar irradiation at 120 °C).

thermo-catalytic activity decreased by about 10%. This can be ascribed to the adsorption of carbonaceous species that can be deposited on the sample surface due to the photothermo-catalytic runs that hindered the absorption of solar light, blocking also the surface-active sites of the catalyst.[16,28] For this reason, before the fourth run, the sample surface was cleaned under UV irradiation using a mercury lamp (100 W, Black-Ray B-100A, 365 nm) in a He stream for 2 h in order to desorb the possible impurities and the carbonaceous species. Subsequently, under irradiation, water vapour was introduced along with the He stream. In parallel, the gas exiting the reactor was analyzed by GC-TCD to assess the effectiveness of the process of cleaning, as UV/UV-A surface cleaning is typically performed prior to conducting photocatalytic tests[29] and also the fresh sample was pretreated in this way before the photothermo-catalytic measurements (see the Experimental section). This further surface cleaning step was effective, leading to the reactivation of the catalyst. In fact, when the cleaned sample underwent simulated solar irradiation, it was able to reach the same activity as the first run (Fig. 2). Importantly, the presence of Ni (Table 1) favored the formation of methane instead of CO (Fig. 2). In fact, Ni-based catalysts are largely explored in the literature for CO_2 conversion in photocatalytic, photothermo-catalytic, and thermal catalytic approaches.[16,30] The performance of Ni-based samples approached those of more expensive noble metal-based catalysts;[26] furthermore, Ni-based materials also showed interesting properties under irradiation with significant visible light absorption in the UV–vis region and the surface plasmon resonance effect.[31]

However, also the presence of other metals, such as Co, Mn and Cu (Table 1), can affect the photothermo-catalytic activity. In particular, Co not only promotes CO_2 activation but also plays a key role in enhancing the H_2O oxidation reaction (water vapor added as a reducing agent as described in section 2.2) with the formation of the necessary protons required for CO_2 photothermo-catalytic reduction.[24,32] The presence of Mn ions is useful to enhance CO_2 adsorption because, due to their redox properties (improved by the photothermal approach), they favor the formation of oxygen vacancies (preferential sites for CO_2 adsorption), also enhancing charge carriers separation.[33,34]

Finally, also the presence of Cu can promote CO_2 conversion due to its capability to favour electron mobility, decreasing in this way the kinetic barriers for CO_2 reduction.[35–37]

Due to the results obtained after 5 runs (for a total of 20 h of simulated solar irradiation at 120 °C), to further test the stability of the employed photothermo-catalyst, longer tests for 20 runs were performed (Fig. 3). In this case, each run lasted 15 h (for a total of 300 h of simulated solar irradiation at 120 °C), because, as explained before, after 15 h, the sample started to lose activity (Fig. 2). Consequently, every 15 h, the surface of the sample was cleaned with UV irradiation following the procedures reported above.

Interestingly, with these treatments, the catalyst showed good stability without significant decreases in activity (Fig. 3). Consequently, due to the longer irradiation time of heating/irradiation, the CO_2 conversion increased from the 64% obtained after 5 h (Fig. 2) to 85% obtained after 15 h (Fig. 3, first run) with also a linear enhancement in CH_4 and CO formation.

The point is that, with regular surface cleaning treatments, the sample can be used as a photothermo-catalyst even in long-term tests. From a practical point of view, the UV pre- and post-treatments could be replaced using amplified solar light treatments (by means of solar collectors, parabolic compound reactors[38] or high-power solar simulators). Considering that the solar irradiation contains 5% UV irradiation, that the incident irradiation will be amplified and that a possible scale-up system will work in continuous mode instead of under batch conditions, the treatment with a high flow of an inert gas com-

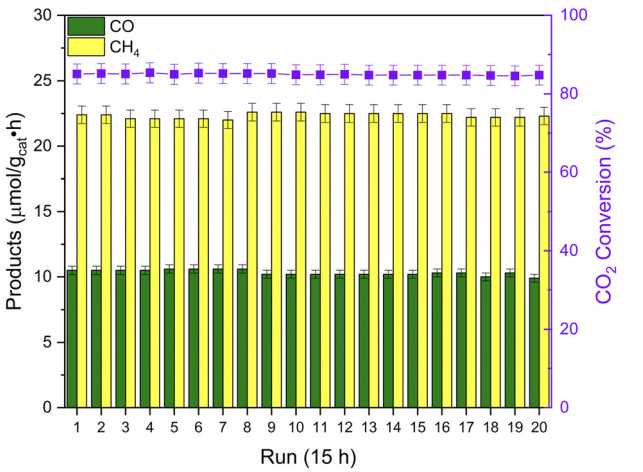

Fig. 3 Solar photothermo-catalytic tests for 20 runs (each run = 15 h of simulated solar irradiation at 120 °C). At the end of each run, the sample was irradiated with a UV lamp for 2 h under a He flow to remove the possible contaminants and the adsorbed carbonaceous species.

Table 2 Comparison of the results of the solar photocatalytic or solar photothermo-catalytic CO_2 reduction reaction, obtained from the new malate phases and other catalysts

Catalyst	Experimental conditions	CO_2 conversion (%)	CO selectivity (%) and formation rate (μmol/g_{cat}•h)	CH_4 selectivity (%) and formation rate (μmol/g_{cat}•h)	TON	Ref.
New malate compound	Solar lamp (300 W, 10.7 mW cm^{-2}), T = 120 °C, t irradiation = 5 h, g_{cat} = 0.2 g; reactant gases: CO_2 (99.999%) and H_2O vapour	64	18% (7.9)	82% (12.8)	1.33[a] (CH_4)	This work
Synthesized phyllosilicate-Ni/Ce@CeO_2	Solar lamp (300 W, 10.7 mW cm^{-2}), T = 120 °C, t irradiation = 5 h, g_{cat} = 0.2 g; reactant gases: CO_2 (99.999%) and H_2O vapour	87	74% (15.8)	26% (5.6)	—	16
Cu_2O/TiO_2-MOR zeolite	Solar lamp (300 W, 10.7 mW cm^{-2}), T = 120 °C, t irradiation = 5 h, g_{cat} = 0.2 g; reactant gases: CO_2 (99.999%) and H_2O vapour	65	75% (12.3)	25% (4.1)	—	15
$CoCuO_x/TiO_2$–CeO_2	Solar lamp (300 W, 10.7 mW cm^{-2}), T = 120 °C, t irradiation = 5 h, g_{cat} = 0.2 g; reactant gases: CO_2 (99.999%) and H_2O vapour	60	87% (12.0)	13% (1.8)	—	24
Ni/0.5-TiO_2@NC	Xe lamp (300 W, 1200 mW cm^{-2}), T = 275 °C, t irradiation = /, g_{cat} = 0.16 g; reactant gas: CO_2 18.7%, H_2 70.5%, N_2 10.8%	70	—	99% (60.0)	—	39
Cu–Ni/TiO_2	Xe lamp (300 W, 200 mW cm^{-2}), t irradiation = 5 h, g_{cat} = 0.005 g; reactants: CO_2, 1 mL of water	—	4% (1.0)	96% (60.0)	—	40
Pt/MnO_x	Xe lamp (300 W), g_{cat} = 0.06 g; reactants: $NaHCO_3$ + H_2SO_4	—	25% (45.0)	75% (75.0)	—	41
Bi-NCs/Bi_2O_3	Xe lamp (300 W with a cutoff filter of 420 nm), t irradiation = 4 h, g_{cat} = 0.015 g; reactants: CO_2, 1 mL of water	—	18% (1.5)	82% (30.0)	—	42
Porphyrin-based porous organic polymers ((POP)_1)	Long-arc Xe lamp (500 W, 106 mW cm^{-2}), g_{cat} = 0.01 g, dispersed in MeCN : H_2O : TEOA = 12 mL : 3mL : 3 mL solution. reactant: CO_2	—	— (518)	—	—	4
Zn@BP-POP	Xe lamp (300 W, 320–780 nm, 100 mW cm^{-2}), g_{cat} = 0.005 g dispersed in deionized water; reactant: water-vapor-saturated CO_2 gas	—	— (43)	—	34.6	5
Co-POP	Xe lamp (450 W with UV cut-off filter), g_{cat} = 0.005 g dispersed in deionized water; reactant: CO_2	—	— (145.7)	—	—	6

[a] The TON calculation could be understated and not comparable with those of other samples in the literature, considering also the complexity of the here examined sample and the hybrid catalytic approach (photothermo-catalysis). For the calculation, it was assumed that the whole measured BET surface area was equal to the number of active sites. It is important to highlight that Ti, Mn, Bi, and Ce are CRMs.

bined with amplified solar irradiation could guarantee effective cleaning of the sample surface.

Table 2 provides a comparative overview of the catalytic results achieved under solar-driven photothermal or photocatalytic conditions alongside several catalysts evaluated under analogous experimental settings,[15,16,24] also with catalysts available in the literature.[4–6,39–42] It is fundamental to note that a quantitative comparison of the data is challenging to evaluate due to (i) the chemical compositions of the examined catalysts, which are different; (ii) the diversity of experimental configurations and reaction conditions; and (iii) the potential formation of additional CO_2 reduction products beyond CO and CH_4. Nevertheless, the tested sample showed a promising CO_2 conversion performance, with an enhanced CH_4 selectivity compared to other catalysts reported in the literature (Table 2). It is important to underline however that the reported data here showed a low CO and CH_4 production rate with a consequent low turnover number (TON) especially if compared with other organic/inorganic-based samples such as porphyrin-based porous organic polymers (POPs).[4–6] Therefore, the optimization of the reaction conditions and the catalyst synthesis is required. Nonetheless, these preliminary results are hopeful in order to propose a sustainable photothermo-catalyst in the context of circular economy and waste valorization.

As largely reported, in fact, the Ni/TiO_2-based samples showed a CH_4 selectivity of >95%.[39,40] Since 2021, titanium has been classified as a CRM by the European Union, making the search for suitable alternatives a pressing priority. Also, Ce, Mn, and Bi are in the list of CRMs. In this context, the investigated sample shows significant promise, particularly given its origin from waste materials. This not only enhances the sustainability of the process but also aligns with circular economy principles, where a waste material finds a second life in another application or process. The approach integrates the utilization of a greenhouse gas (CO_2) to produce solar fuels under mild, energy-efficient conditions, using a catalyst derived from recycled materials, thus promoting an environmentally friendly and resource-conscious solution.

The textural properties of the malate material were examined by N_2 physisorption measurements. The sample exhibited a type III isotherm with an H3 hysteresis loop (Fig. 4) associated with the presence of slit-shaped pores.[43] The BET surface

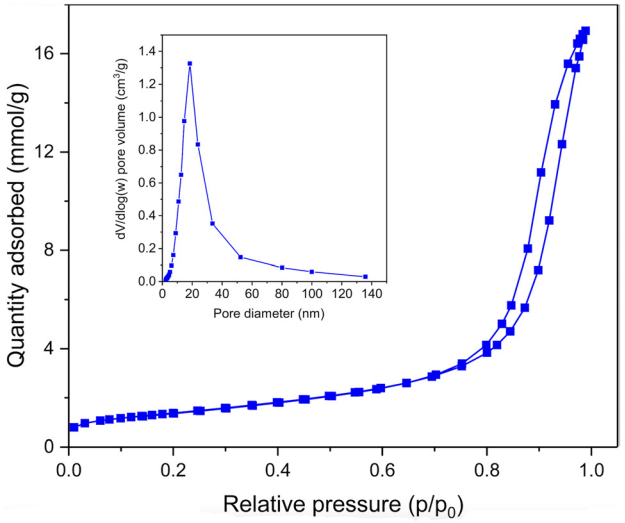

Fig. 4 N_2 isotherm curve of the malate material. The inset shows the BJH pore size distribution.

area was 121 m^2 g^{-1}, whereas the mean pore diameter was 18.5 nm, with the main presence of mesopores (2–50 nm) and some macropores (>50 nm). The measured value of the surface area is similar to those of other mixed oxides/metal-supported oxide catalysts, whose porosity facilitates CO_2 adsorption and subsequent conversion.[16,28,32]

Fig. 5 shows the XRD patterns of the catalyst before and after its fifth run of photothermal activity. Before the functional tests, only the $MH_2(C_4H_4O_5)_2{\cdot}4H_2O$ phase can be detected[21] (Fig. 5a and b). Following the catalytic tests, the XRD pattern revealed two broad halos, indicating the material's transition to an amorphous state (Fig. 5a–c). 2D XRD images collected at the synchrotron are also reported in Fig. 5, showing a uniform grain distribution along the Debye rings for the crystalline sample and highlighting the amorphous nature of the malate after the catalytic tests. This structural transformation is particularly significant, as it demonstrates the material's amorphization during functional testing, which may explain the results of functional tests.

Generally, improving catalyst performance can follow two main strategies. The first focuses on increasing the number of available active sites, often achieved by engineering the catalyst's morphology to expose a larger surface area. The second approach aims to boost the intrinsic activity at each active site by tailoring the local atomic structure and modifying electronic properties. Notably, amorphous materials—characterized by long-range disorder but short-range atomic order—offer distinct advantages over crystalline materials, especially if the material is used in photocatalysis or in hybrid catalytic approaches. Their benefits include a greater density of active sites, a wider range of chemical compositions, and enhanced structural adaptability,[44] but still little research has been done in this field. There is ongoing discussion concerning how structural disorder contributes to enhanced catalytic activity. This activity might result from particular metal ion coordination or oxidation states, bulk or surface defects and vacancies in amorphous materials, catalyst domains at the sub-nanometer scale, or the existence of an increased number of active sites.[45]

However, only a limited number of studies have specifically explored these aspects in catalyst behavior. This is due to the difficulty of investigating amorphous materials with conventional characterization techniques.

The atomic pair distribution function (PDF) method, representing the Fourier analysis of total scattering data that can be collected by means of dedicated synchrotron beamlines, is a unique probe that provides information on intermediate-range structures, since the main power of the PDF is its capacity to describe deviation from perfect periodicity. Fig. 6 shows the

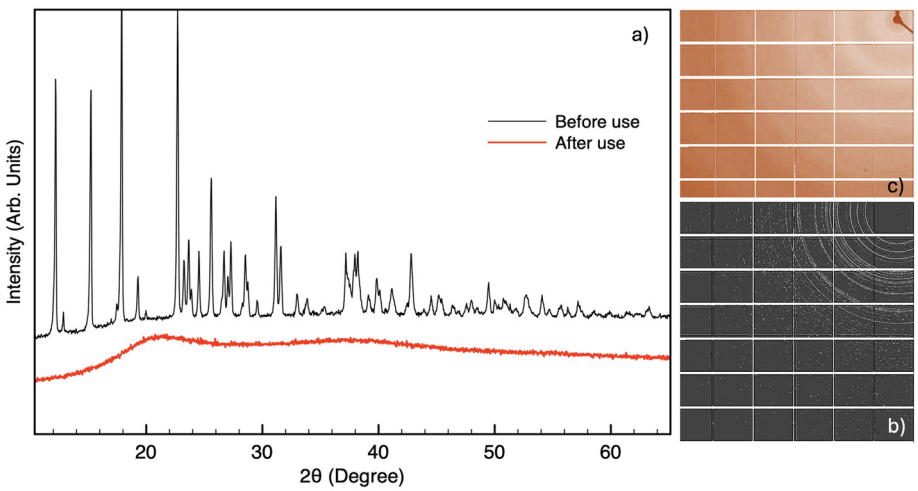

Fig. 5 (a) XRD patterns of the malate material before (black line) and after (red line) the photothermo-catalytic tests. Before the functional test, all the peaks in the XRD pattern can be attributed to the newly detected phase $MH_2(C_4H_4O_5)_2{\cdot}4H_2O$, with M representing the metals. 2D images of XRD patterns of the malate phase (b) before and (c) after photocatalytic tests collected under synchrotron radiation are also shown.

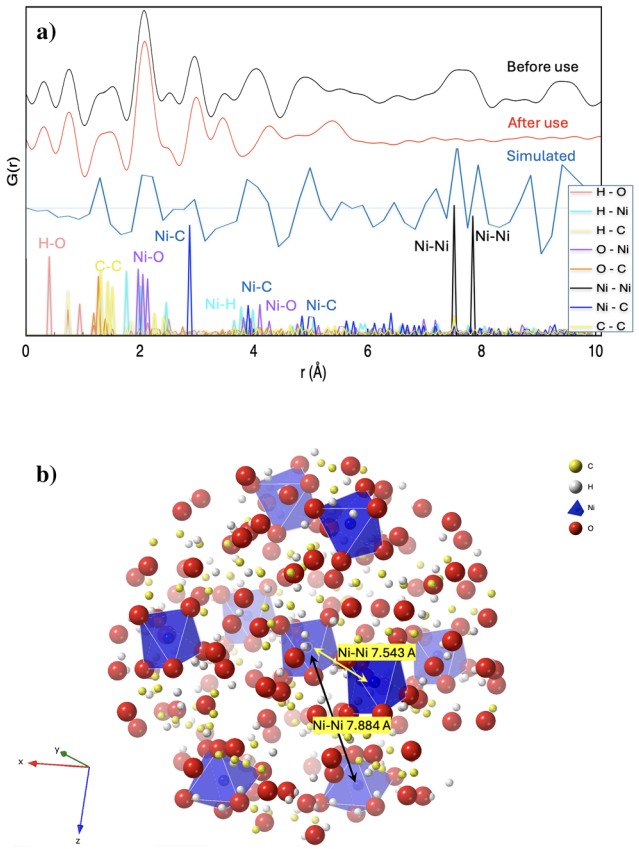

Fig. 6 (a) Pair distribution function (PDF), obtained by Fourier analysis of total scattering data collected under synchrotron radiation, for the malate sample before and after catalytic tests. The simulated PDF curve for the malate crystalline structure, obtained using CrystalMaker software, is also reported. (b) Molecular model of the malate phase, obtained using CrystalMaker software. The Ni–Ni distances of different malate molecules, corresponding to the medium-range order of the crystal, are highlighted. The simulation was performed by considering a full Ni occupancy instead of the exact M composition.

PDF of the malate sample, obtained before and after catalytic tests; also, the malate structure is reported. Well-defined PDF peaks can be observed for both samples up to about 6 Å. They are related to the atoms in the coordination structure, with the peak position depending on the atoms' separation. A simulation of the PDF pattern was realized by using CrystalMaker X and the corresponding atomic distances that resulted in the PDF peaks were highlighted (Fig. 6a). The simulated PDF is in good agreement with the experimental data, even if for simplicity, the Ni occupancy was set equal to 1. Indeed, slight changes in Ni occupancy, to take into account the exact composition of the malate phase (only Ni, representing the central atom, is considered for M in the malate chemical formula), are not able to produce substantial changes in the simulated PDF. Comparing the PDF data before and after catalysis, it is found that there is basically no change in the peak position before 4 Å. Indeed, the observed local correlation for hydrogen and carbon atoms at distances less than 2.0 Å is maintained. The local correlations of Ni–C (at 2.8 Å and 3.9 Å) and Ni–O (at the distances of about 2 Å) indicate that atoms maintained their relative arrangement surrounding the nickel center, confirming the well-preserved malate core structure. It is important to note that the PDF analysis was conducted on the mixed-metal malate compound before and after catalysis and not on separate compounds containing only one type of metal ion. As a result, the observed PDF reflects an average of the local structures around the various metal centers. Given that Ni is the dominant metal species (Table 1), the peaks primarily correspond to Ni–O and Ni–C correlations, while the contributions from Co, Mn, and Cu are less pronounced due to their lower abundance. This averaging effect can mask the individual metal–oxygen or metal–metal distances (*e.g.*, Co–O, Mn–O, or Cu–O), which are expected to differ from those of Ni. To resolve these specific contributions, it would be necessary to synthesize and analyze single-metal malate compounds for comparison. Nevertheless, the current results show that the malate structure remains locally stable during catalysis, as indicated by the preservation of short-range correlations in the averaged PDF profile.

The most evident structural change in the PDF is the disappearance of the peaks attributed to the Ni–Ni correlation, at about 7.5 and 7.9 Å (see Fig. 6), indicating a collapse of the crystalline structure at medium-range order, even if the local short order is preserved.

The sample amorphization can be attributed to the release of water molecules from the structure, as confirmed by thermogravimetric analysis (TGA) results, with a collapse of the medium structural order that is not significant for the Ni local structure (see Fig. 6b). This is an interesting result because no similar behavior is described in the available literature. Only a few papers report that a catalyst can change its structure during the reactions.[45] In particular, and concerning Ni catalysts, it was recently reported that amorphous Ni particles show unexpectedly high performance in comparison with the corresponding crystalline phases.[46] This amorphization, induced by partial dehydration, leads to a structurally disordered yet chemically conserved form of the malate, which may expose additional active sites and increase structural flexibility—factors that can plausibly enhance catalytic performance. Then, the disorder introduced by amorphization also in the investigated reaction plays a beneficial role in promoting the photothermo-catalytic activity, possibly by enhancing active site availability and reactivity. In addition, because amorphous Ni catalysts facilitate the activation of CO_2 more efficiently than crystalline Ni, reducing the energy barrier for CO_2 dissociation,[44] it is reasonable to suppose that the amorphization of the material during the CO_2 conversion reaction enhances CO_2 activation, making the reaction more efficient under photothermal conditions. Amorphous materials lack the rigid, periodic lattice structure of crystalline catalysts, which can result in greater structural flexibility and adaptability to reaction conditions. Furthermore, the amorphization of the catalyst can also modulate the local electronic state, thus optimizing the carrier transfer pathway and strongly influencing the catalyst selectivity.[47,48] The disordered atomic

arrangement allows the formation of free active sites for adsorption, activation, and stabilization of molecules such as CO_2. For these reasons, Ni can efficiently activate CO_2 and the simultaneous presence of other metals (Co, Mn, and Cu) led to exploiting their co-catalyst features, improving electron mobility, solar light absorption, and CO_2 interaction.[30,34,36]

Carbon dioxide was therefore adsorbed in the additional active sites generated by the amorphization of the malate compound and successively converted by the combined action of the metals. This peculiar catalyst structure led to good photothermal stability, even though the reaction was performed several times (Fig. 2 and 3).

Fig. 7 shows the SEM images of the malate sample before and after the catalytic tests (five runs). The results of EDS analysis are also reported in terms of metal ratios for a comparison.

SEM images allow us to observe the morphology of the sample before and after the photothermo-catalytic test (Fig. 7a and b, respectively). Although the morphology in the two images (Fig. 7a and b) appears quite similar, with particles of a few microns alongside smaller, more fragmented ones, the particle surfaces are relatively smooth before the catalytic tests, and individual particle boundaries remain clearly distinguishable. In contrast, after the catalytic reaction, the material appears more fragmented: the surface has undergone some morphological changes, with some larger particles still present but exhibiting signs of corrosion. This transformation aligns with the observed amorphization of the material, suggesting structural modifications induced by the catalytic process. As a result, the observed catalytic performance can be attributed to the unique coordination environment of the metal ions within the malate complex, which facilitates CO_2 activation and subsequent conversion. Notably, the mean EDS analysis (Fig. 7c) reveals a metal ratio that aligns well with the chemical analysis results presented in Table 1. However, slight local deviations from the nominal composition are observed when analyzing different particles, which may be attributed to minor variations in the local metal occupancy. This cannot be highlighted by X-ray scattering techniques.

To complement the experimental results, the preliminary sustainability analysis of the synthesized malate-based catalyst was evaluated using a rapid assessment framework that relies

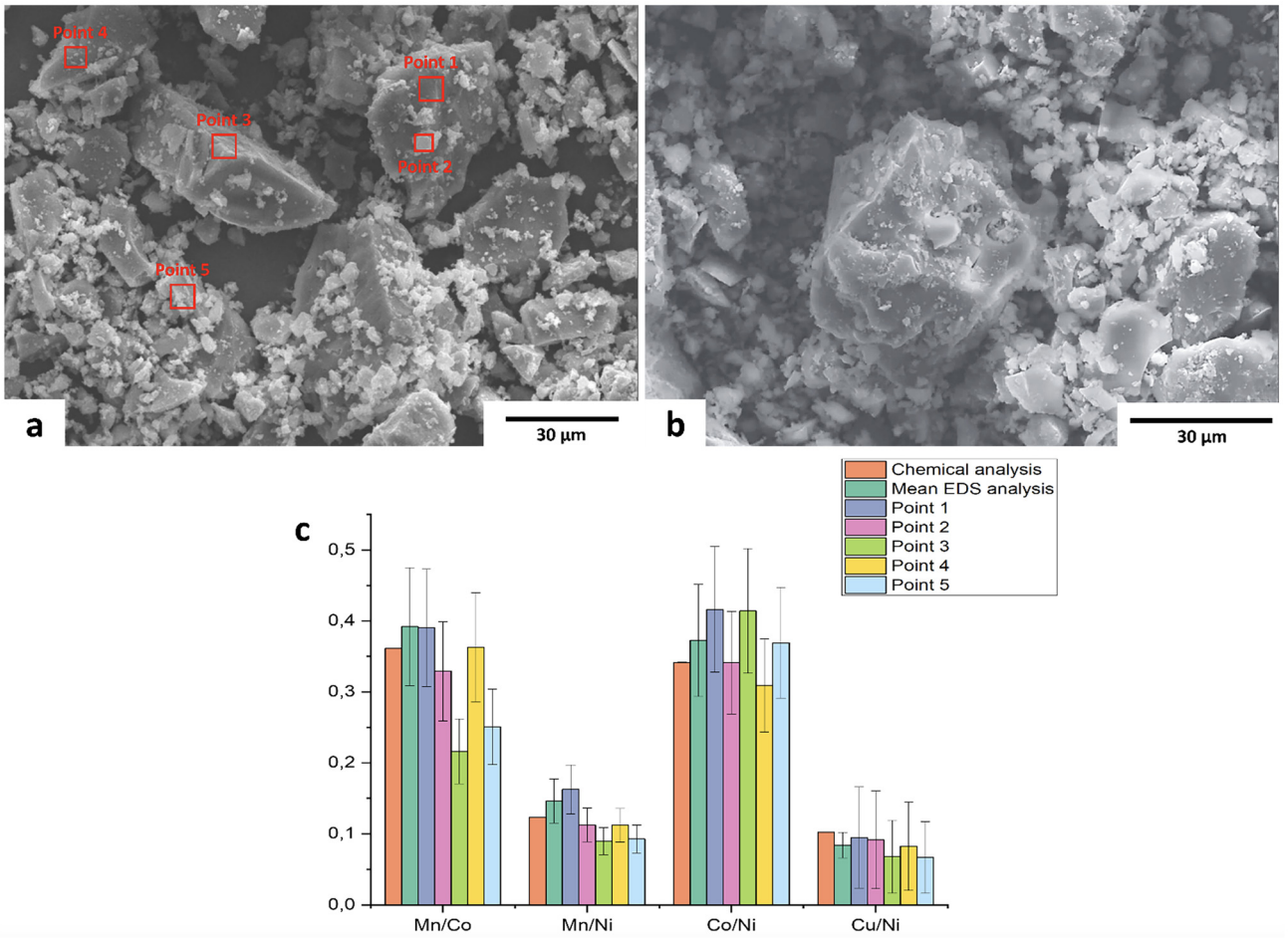

Fig. 7 SEM images (a) before and (b) after use for photocatalytic tests and (c) metal ratio, based on the chemical composition (Table 1) and EDS analyses.

on two key indicators: embodied energy (EE) and carbon footprint (CF),[49,50] representing the required energy for the material synthesis and the associated CO_2 emissions. In particular, the EE quantifies the total energy required for material production, from raw material extraction to final synthesis, while CF measures the associated greenhouse gas emissions. By applying this method, we were able to benchmark the environmental impact of the new catalyst against some conventional materials used in catalysis (some of them are reported in Table 2), offering valuable insights into its potential for sustainable application in CO_2 conversion processes. Fig. 8 shows a logarithmic plot comparing the EE (MJ kg^{-1}) and CF (kg_{CO_2eq} kg^{-1}) of some materials used as catalysts for the same application, including anatase, maleic anhydride, cerium oxide, and the newly developed malate compound under different recovery scenarios (10%, 50% and 100%). It is important to highlight that the EE and CF for the reported materials are extracted from the ecoinvent v3.8 and Environmental Footprint (provided under the guidance of the European Commission and its Joint Research Centre in its newest version 3.1 of March 2024) databases; therefore, they refer to the bulk materials. In some cases, to obtain catalysts, some particular treatments are mandatory, including purification, impregnation, and subsequent calcination (with temperatures of about 900 °C), key steps for obtaining the required catalytic performance,[51] with the result of increasing the associated EE and CF (not considered in this figure). In addition, the elements contained in the comparison materials are all included in the CRMs list. In the literature and available databases, EE and CF values for bismuth oxide, commonly used as a catalyst, are not reported. Therefore, the EE and CF values of metallic bismuth were considered instead. The values shown in Fig. 8 for cerium oxide, anatase, and bismuth represent average estimates, with ranges reflecting the variability associated with different production methods. Specifically, for cerium oxide, EE values range from 204 to 383 MJ kg^{-1} and CF values from 16.5 to 26.1 kg_{CO_2eq} kg^{-1}; for anatase, EE ranges between 56.2 and 92.5 MJ kg^{-1} and CF between 4.45 and 7.75 kg_{CO_2eq} kg^{-1}, while for bismuth, EE varies from 138 to 350 MJ kg^{-1} and CF from 8.63 to 19 kg_{CO_2eq} kg^{-1}. It should be noted that, since additional processing steps are required to obtain bismuth oxide from metallic bismuth, the actual EE and CF values of the oxide are expected to be higher than those reported here.

For the new malate, all the synthesis steps have been accounted for. This compound exhibits progressively lower environmental impacts as the recovery rate increases, moving closer to the lower-impact region occupied by malic acid and anatase.

This figure highlights the environmental advantage of the malate compound when produced with efficient recovery. This result can also be optimized if malic acid is extracted from waste food, reducing the EE and CF of this acid. In addition, the proposed treatment was conducted under laboratory conditions; however, when scaled to industrial processes using large-scale ovens, the overall energy consumption for the treatment is expected to be significantly lower.

This analysis emphasizes the sustainability potential of the malate catalyst, especially when maximizing recovery from recycled sources.

Table 3 summarizes and integrates the advancements in green chemistry introduced through this work, highlighting how each sustainable strategy adopted aligns with specific green chemistry principles, including waste prevention, use of renewable feedstocks, energy efficiency, safer chemical design, and improved atom economy.

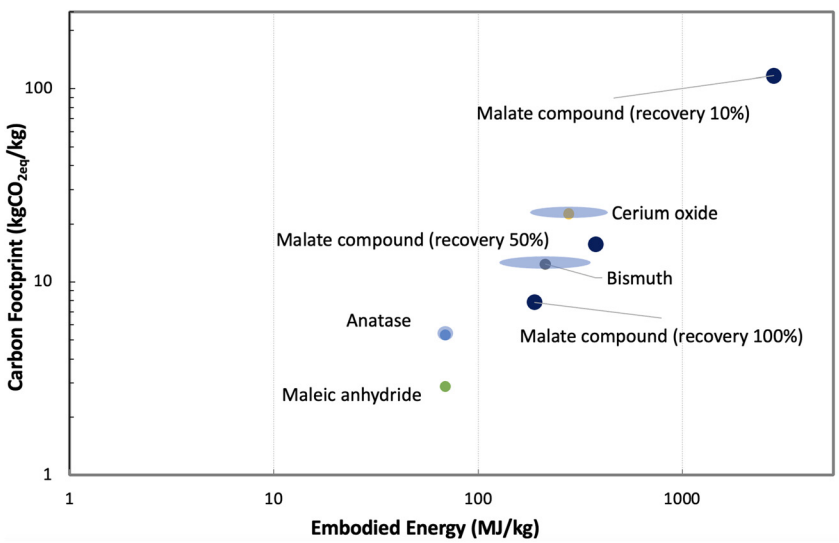

Fig. 8 EE and CF of some materials used for catalysis, containing CRMs. For the new malate phase, the evaluation was realized considering laboratory synthesis conditions and at different recycling rates. Data for the other materials are extracted from the ecoinvent v3.8 and Environmental Footprint (provided under the guidance of the European Commission and its Joint Research Centre in its newest version 3.1 of March 2024) databases. For cerium oxide, anatase, and bismuth, EE and CF values are reported as average values, and the variability range is represented.

Table 3 Summary of the advancements in green chemistry enabled by this work

Sustainable strategy implemented in the study	Green chemistry principle(s) embodied
1. Recycling of battery-waste residues to make the catalyst (spent LIB black mass → malate phase)	Prevent waste (turning an end-of-life stream into a feedstock rather than disposing of it).
2. Use of solar light to drive the photothermo-catalytic reaction	Increase energy efficiency (reaction proceeds at 120 °C using free, abundant solar photons instead of high-temperature furnace heating). Prefer catalysis (solar photothermo-catalysis lowers the energy barrier).
3. Use of L-malic acid instead of inorganic acid for the synthesis of the new catalyst	Use renewable feedstocks – L-malic acid (that may also be extracted from food waste).
4. Substitution of critical raw materials (Ti, Ce, and Bi) with a new polymetallic malate	Design safer chemicals (replace scarce/strategic or potentially more toxic CRMs with a malate compound). Design less hazardous syntheses (no Ti-, Bi- or Ce-based oxide calcination (see Table 2); the new pathway uses mild leaching and room-temperature precipitation). Prefer catalysis (the new catalyst retains high activity without CRMs).
5. Valorization of CO_2 into CH_4 and CO ('solar fuels')	Prevent waste (CO_2 viewed as a feedstock, not an emission). Maximize atom economy (most C atoms from CO_2 end up in CH_4/CO).

4. Conclusions

This study investigates a newly discovered malate-based catalyst, derived from spent lithium-ion battery recycling, demonstrating its promising performance in photothermocatalytic CO_2 conversion. The research highlights the potential of integrating new material development with sustainable waste valorization, laying the foundation for the design of environmentally friendly catalytic solutions not based on CRMs.

By combining recycling and catalysis, this work exemplifies a transformative pathway aligned with circular economy principles. Repurposing battery waste into high-value catalysts not only advances green chemistry goals but also promotes more resource-efficient chemical processes. Notably, the application of the pair distribution function (PDF) method enabled, for the first time, a detailed understanding of catalyst amorphization and its positive impact on performance. Using X-ray scattering techniques, the study reveals a key transformation: a shift from a crystalline resting state to an active amorphous shell around the crystallites—an insight that offers valuable guidance for the possible design of more efficient and durable catalysts. Furthermore, the successful application of this catalyst bridges the gap between AI predictions and experimental validation. A preliminary sustainability analysis allows us to conclude that the energies and emissions associated with this new material synthesis are comparable to those involved in the production of traditional materials, like ceria and titania, but Ti and Ce are on the list of CRMs.

Overall, this research sets the stage for future studies aimed at optimizing the reaction conditions, the reactor design, and the catalyst performance and at deepening the correlation between this hybrid catalysis (photothermo-catalysis) with the peculiar properties of the here examined malate compound. The possibility to exploit in a green circular way the waste material recycling processes to obtain high-added-value catalysts alternative to the most commonly used CRMs, favoring also the conversion of CO_2 into solar fuels, is a promising way to increase the overall sustainability of the industrial processes with the possibility of reducing resource expenditure.

Author contributions

Antonella Cornelio: data curation and writing – original draft. Alessandra Zanoletti: data curation, formal analysis and investigation. Giusy Dativo: data curation, formal analysis, investigation, and visualization. Roberto Fiorenza: conceptualization, data curation, investigation, methodology, supervision, validation, writing – original draft, and writing – review & editing. Annalisa Zacco: formal analysis and visualization. Mohsin Muhyuddin: formal analysis and visualization. Carlo Santoro: formal analysis and visualization. Laura E. Depero: data curation and analysis and writing – review & editing. Elza Bontempi: conceptualization, data curation and analysis, investigation, methodology, project administration, resources, supervision, validation, visualization, writing – original draft, and writing – review & editing.

Conflicts of interest

The authors declare that they have no known competing financial interests or personal relationships that could have appeared to influence the work reported in this paper.

Data availability

The data supporting this article have been included in the manuscript.

Acknowledgements

This work was supported by MUR in the frame of the FISA 2022 call, through the project CARAMEL ("New CArbothermic approaches to Recovery criticAL MEtals from spent Lithium-ions batteries" – CUP D73C24000220001). Alessandra Zanoletti acknowledges financial support from the Next-GenerationEU (Italian PNRR – M4 C2, Invest 1.3 – D. D. 1551.11-10-2022, PE00000004, CUP D73C22001250001) within the MICS (Made

in Italy – Circular and Sustainable) extended partnership for her research fellowship.

We acknowledge the European Synchrotron Radiation Facility (ESRF) for the provision of synchrotron radiation facilities and momentum transfer for facilitating the measurements. Jakub Drnec is thanked for assistance and support in using beamline ID31. The measurement setup was developed with funding from the European Union's Horizon 2020 Research and Innovation program under the STREAMLINE project (grant agreement ID 870313). Measurements performed as part of the MatScatNet project were supported by OSCARS through the European Commission's Horizon Europe Research and Innovation programme under grant agreement no. 101129751. The authors thank Eneris Group for black mass sample supply. We dedicate the paper to the birth of Alberto Levrangi.

References

1 O. Emmanuel, Rozina and T. C. Ezeji, *Next Sustainability*, 2025, **6**, 100108.
2 A. Zanoletti, B. M. Bresolin and E. Bontempi, *Global Challenges*, 2024, **8**, 2400250.
3 S. H. Choi, I. Song and W. J. Dong, *Energy Mater.*, 2025, **5**, 500062.
4 A. Boruah, B. Boro, J. Wang, R. Paul, R. Ghosh, D. Mohapatra, P. Z. Li, X. Zhang and J. Mondal, *ACS Appl. Mater. Interfaces*, 2024, 1259–1272.
5 A. Boruah, B. Boro, R. Paul, C. C. Chang, S. Mandal, A. Shrotri, C. W. Pao, B. K. Mai and J. Mondal, *ACS Appl. Mater. Interfaces*, 2024, **16**, 34437–34449.
6 R. Paul, R. Das, N. Das, S. Chakraborty, C. W. Pao, Q. T. Trinh, G. T. K. K. Gunasooriya, J. Mondal and S. C. Peter, *Angew. Chem.,– Int. Ed.*, 2023, **62**, e202311304.
7 H. Jiang, J. Shen, L. Sun, J. Li, W. Wang, L. Wang and Q. Liu, *Green Chem.*, 2025, **27**, 6989–7008.
8 X. Liu, C. Cui, S. Wei, J. Han, X. Zhu, Q. Ge and H. Wang, *Green Chem.*, 2024, **26**, 531–541.
9 S. Rodríguez-Jiménez, E. Lam, S. Bhattacharjee and E. Reisner, *Green Chem.*, 2023, **25**, 10611–10621.
10 J. Sakizadeh, J. P. Cline, E. Wolfe, R. Thorpe, M. A. Snyder, C. J. Kiely and S. McIntosh, *Green Chem.*, 2023, **25**, 566–578.
11 X. Wen, X. Geng, G. Su, Y. Li, Q. Li, Y. Yi and L. Liu, *Green Chem.*, 2025, **27**, 4898–4925.
12 R. Ma, J. Sun, D. H. Li and J. J. Wei, *Int. J. Hydrogen Energy*, 2020, **45**, 30288–30324.
13 B. Guene Lougou, B.-X. Geng, R.-M. Pan, W. Wang, T.-T. Yan, F.-H. Li, H. Zhang, O. S. Djandja, Y. Shuai, M. Tabatabaei and D. Sabi Takou, *Rare Met.*, 2024, **43**, 2913–2939.
14 S. N. Habisreutinger, L. Schmidt-Mende and J. K. Stolarczyk, *Angew. Chem., Int. Ed.*, 2013, **52**, 7372–7408.
15 R. Fiorenza, C. Contarino, V. Spanò, M. T. A. Iapichino and S. A. Balsamo, *Catal. Today*, 2023, **423**, 114251.
16 G. Dativo, E. L. Greca, L. F. Liotta, V. L. Parola, M. Condorelli, G. Impellizzeri, G. Compagnini, S. Sciré and R. Fiorenza, *J. CO2 Util.*, 2024, **82**, 102765.
17 A. Cornelio, E. Galli, M. Scaglia, A. Zanoletti, A. Zacco, A. Bonometti, G. Magugliani, E. Mossini, E. Macerata, S. Federici and E. Bontempi, *Energy Storage Mater.*, 2024, **72**, 103703.
18 A. Fahimi, I. Alessandri, A. Cornelio, P. Frontera, A. Malara, E. Mousa, G. Ye, B. Valentim and E. Bontempi, *Resour., Conserv. Recycl.*, 2023, **194**, 106989.
19 A. Cornelio, A. Zanoletti, M. Scaglia, E. Galli, D. L. Corte, G. Biava and E. Bontempi, *RSC Sustainability*, 2024, **2**, 2505–2514.
20 Proposal for a REGULATION OF THE EUROPEAN PARLIAMENT AND OF THE COUNCIL establishing a framework for ensuring a secure and sustainable supply of critical raw materials and amending Regulations (EU) 168/2013, (EU) 2018/858, 2018/1724 and (EU) 2019/1020 Brussels, 2023.
21 A. Zanoletti, A. Cornelio, E. Galli, M. Scaglia, A. Bonometti, A. Zacco, L. E. Depero, A. Gianoncelli and E. Bontempi, *Environ. Res.*, 2025, **267**, 120709.
22 A. Zanoletti, A. Cornelio, L. Borgese, G. Siviero, A. Cinosi, E. Galli and E. Bontempi, *J. Environ. Manage.*, 2025, **380**, 124973.
23 P. Juhás, T. Davis, C. L. Farrow and S. J. L. Billinge, *J. Appl. Crystallogr.*, 2013, **46**, 560–566.
24 R. Fiorenza, M. Bellardita, S. A. Balsamo, L. Spitaleri, A. Gulino, M. Condorelli, L. D'Urso, S. Scirè and L. Palmisano, *Chem. Eng. J.*, 2022, **428**, 131249.
25 E. Karamian and S. Sharifnia, *J. CO2 Util.*, 2016, **16**, 194–203.
26 L. Patron, O. Carp, I. Mindru, G. Marinescu and E. Segal, *J. Therm. Anal. Calorim.*, 2003, **72**, 281–288.
27 J. Thomas, A. Lincy, V. Mahalakshmi and K. V. Saban, *Crystallogr. Rep.*, 2013, **58**, 93–97.
28 G. Dativo, M. Condorelli, G. Compagnini, G. Impellizzeri, S. Scirè and R. Fiorenza, *Discover Appl. Sci.*, 2025, **7**, 186.
29 M. Dilla, R. Schlögl and J. Strunk, *ChemCatChem*, 2017, **9**, 696–704.
30 A. Gouda, K. Hannouche, A. Mohan, C. Mao, E. Nikbin, A. Carrière, J. Ye, J. Y. Howe, M. Sain, M. Hmadeh and G. A. Ozin, *Nat. Commun.*, 2025, **16**, 695.
31 S. Kim, J. M. Kim, J. E. Park and J. M. Nam, *Adv. Mater.*, 2018, **30**, 1704528.
32 R. Fiorenza, L. Calantropo, E. L. Greca, L. F. Liotta, A. Gulino, A. Ferlazzo, M. G. Musumeci, G. Proietto Salanitri, S. C. Carroccio, G. Dativo, M. T. Armeli Iapichino, S. Scirè and G. Impellizzeri, *Catal. Today*, 2025, **449**, 115182.
33 J. H. Qin, P. Xu, Y. D. Huang, L. Y. Xiao, W. Lu, X. G. Yang, L. F. Ma and S. Q. Zang, *Chem. Commun.*, 2021, **57**, 8468–8471.
34 D. Chuanchuan, L. Yuling, S. Hao, L. Shuaishuai, S. Qiyuan and L. Xinzeng, *Fuel*, 2025, **384**, 133949.
35 H. Xie, J. Wang, K. Ithisuphalap, G. Wu and Q. Li, *J. Energy Chem.*, 2017, **26**, 1039–1049.

36 R. Fiorenza, M. Bellardita, S. A. Balsamo, A. Gulino, M. Condorelli, G. Compagnini, S. Scirè and L. Palmisano, *Catal. Today*, 2023, **413–415**, 113949.
37 E. Saccullo, V. Patamia, F. Magaletti, G. Dativo, M. Camarda, R. Fiorenza, V. Barbera, G. Floresta and A. Rescifina, *J. CO2 Util.*, 2024, **85**, 102865.
38 R. J. Braham and A. T. Harris, *Ind. Eng. Chem. Res.*, 2009, **48**, 8890–8905.
39 Z. Xiao, P. Li, H. Zhang, S. Zhang, Y. Zhao, J. Gu, Z. Lian, G. Li, J. J. Zou and D. Wang, *J. Colloid Interface Sci.*, 2024, **672**, 642–653.
40 M. Xu, C. Chen, X. Han, W. Hu and B. Li, *Colloids Surf., A*, 2024, **688**, 133676.
41 J. Xiao, C. Chen, S. Chen, H. Liu and T. Peng, *Chem. Eng. J.*, 2021, **425**, 131627.
42 W. Dai, P. Wang, J. Long, Y. Xu, M. Zhang, L. Yang, J. Zou, X. Luo and S. Luo, *ACS Catal.*, 2023, **13**, 2513–2522.
43 M. Thommes, K. Kaneko, A. V. Neimark, J. P. Olivier, F. Rodriguez-Reinoso, J. Rouquerol and K. S. W. Sing, *Pure Appl. Chem.*, 2015, **87**, 1051–1069.
44 T. Guo, L. Li and Z. Wang, *Adv. Energy Mater.*, 2022, **12**, 2200827.
45 A. Bergmann, E. Martinez-Moreno, D. Teschner, P. Chernev, M. Gliech, J. F. De Araújo, T. Reier, H. Dau and P. Strasser, *Nat. Commun.*, 2015, **6**, 8625.
46 Z. Cai, Y. Cai, Z. Wang, S. Liu, X. Liang, H. Ren, Y. Cao, Z. Su, F. Shen, S. Yang, G. Sun, X. Yang, X. Zhang, M. Hu, X. Liu and K. Zhou, *Chem. Eng. J.*, 2024, **498**, 155554.
47 R. Li, S. Yang, Y. Zhang, G. Yu, C. Wang, C. Chen, G. Wu, R. Sun, G. Wang, X. Zheng, W. Yan, G. Wang, D. Rao and X. Hong, *Cell Rep. Phys. Sci.*, 2022, **3**, 100788.
48 Y. Li, Q. Yin, B. Jia, H. Wang, H. Gu, Q. Hu, H. Yang, T. Guo, P. Hu, L. Li, L. M. Liu and L. Guo, *Angew. Chem.,–Int. Ed.*, 2025, **64**, e202505668.
49 E. Bontempi, *Resour., Environ. Sustainability*, 2022, **9**, 100074.
50 A. Fahimi, S. Ducoli, S. Federici, G. Ye, E. Mousa, P. Frontera and E. Bontempi, *J. Cleaner Prod.*, 2022, **338**, 130493.
51 O. E. Medina, A. A. Amell, D. López and A. Santamaría, *Renewable Sustainable Energy Rev.*, 2025, **207**, 114926.